Review of Synthetically Focussed Guided Wave Imaging Techniques with Application to Defect Sizing

Jacob DAVIES, Francesco SIMONETTI, Michael LOWE and Peter CAWLEY, UK
Research Centre for Non-destructive Evaluation, Imperial College London, UK

Abstract. Synthetically focused imaging has been used for some time in the NDE community. The techniques have primarily been directed towards imaging using bulk waves. There has recently been use of SAFT (Synthetic Aperture Focusing Technique) using guided waves in plates. Here, we review three different synthetically focused imaging algorithms for a linear array aperture: CSM (Common Source Method), SAFT and TFM (Total Focusing Method). The resolution of the different techniques is obtained from scalar diffraction theory and then validated by means of a low frequency (50kHz) steel plate experiment using PZT excitation and laser reception of the A0 mode. Imaging of through thickness slits parallel to the array is then discussed.

Introduction

Synthetic aperture imaging has been used for some time in the NDE community employing bulk waves and two dimensional apertures, see, for example, [1]. More recently, imaging techniques have been applied to imaging defects in plates using guided waves. Work by Sicard et al. [2] has used a scanned wedge transducer with excitation at around 3 MHz and a method termed Lamb-SAFT and work by Wilcox [3] has used a circular array at a frequency of around 150 kHz with synthetic focusing and a spatial deconvolution algorithm to improve angular resolution.

Here we assess three commonly used bulk wave imaging algorithms for use with guided wave inspection: Common Source Method (CSM), Synthetic Aperture Focusing Technique (SAFT) [4] and Total Focusing Method (TFM) [5].

We compare the algorithms in response to a point scatterer and to two point scatterers with analytic theory and then validate the findings with data from a thin steel plate experiment using the fundamental flexural mode (A0) at 50 kHz. We then assess the response of the algorithms to through-thickness slits parallel to the array by means of more plate experiments.

Imaging Algorithms

The imaging algorithms presented here are all synthetically focused imaging techniques. That is to say that the focusing is performed after the data acquisition phase. The advantage of this is that the data acquisition time is low since the relevant time traces need only be recorded once. The algorithms are distinguished by their source-receiver geometries used for data acquisition (figure 1). The CSM uses a common source for

excitation and then receives on all elements of the array (figure 1.a). The SAFT uses the pulse-echo data from each array element in turn (figure 1.b). The TFM uses all possible source-receiver pairs: the array transducer elements are fired in turn and a time trace is recorded for each firing at all array element positions. The TFM can be thought of as a collection of common source images from different source positions. Note that although we require the 'full matrix' for the TFM, we actually only need acquire the triangular matrix shown in figure 1.c since the full matrix is symmetric due to reciprocity.

The geometry of the situation is shown in figure 2. The image for point (x,z) is formed, in the time domain implementations, by delaying each time trace by the amount of time that the excited toneburst would take to reach the point (x,z) from the transmitter at location (x_{tx},0) and then return to the receiver at location (x_{rx},0). The image magnitude is then a summation of the delayed time traces. The delay time for a time trace is therefore a function of the image pixel position and the source-receiver combination that was used to produce it. The image magnitude at image point (x,z) is thus:

$$I(x,z) = \left\| \sum_{tx} \sum_{rx} s_{tx,rx}\left(\frac{d_{tx}(x,z)}{v} + \frac{d_{rx}(x,z)}{v} \right) \right\|, \tag{1}$$

where $d_{tx}(x,z) = \sqrt{(x_{tx} - x)^2 + z^2}$; $d_{rx}(x,z) = \sqrt{(x_{rx} - x)^2 + z^2}$; v is the group velocity of the pulse; $s_{tx,rx}$ is the time trace recorded with receiver *rx* from excitation with source *tx*.

For the CSM, the source is the same for all time traces and hence there is no need to sum across *tx*. For the SAFT the source position is the same as the receiver position and hence there is only one summation. For the TFM, we use all the available time traces and hence we need to sum over both the source location (*tx*) and the receiver location (r*x*).

The time domain implementations of the algorithms are sufficient for bulk wave imaging. However, since we are dealing with guided waves then dispersion compensation is needed. One method would be to apply a dispersion compensation post-processing algorithm such as that presented by Wilcox [6] to each time trace prior to running the time-domain imaging algorithms. An easier and quicker method is to run the algorithms directly with dispersion compensation in the frequency domain:

$$I\ (x,z) = \left\| \sum_{tx} \sum_{rx} \sum_{\omega} S_{tx,rx}(\omega) \exp(ik(\omega)\big(d_{tx}(x,z) + d_{rx}(x,z)\big) \right\|, \tag{2}$$

where $k(\omega) = \omega / v_{ph}(\omega)$; $v_{ph}(\omega)$ is the phase velocity; $S_{tx,rx}(\omega)$ is the frequency spectrum of $s_{tx,rx}(t)$. $v_{ph}(\omega)$ can be predicted theoretically for a given geometry using DISPERSE [7]. Note that there is now an extra summation in (2) over frequency. The frequency range chosen is commonly the bandwidth of the main lobe of the input toneburst frequency spectrum.

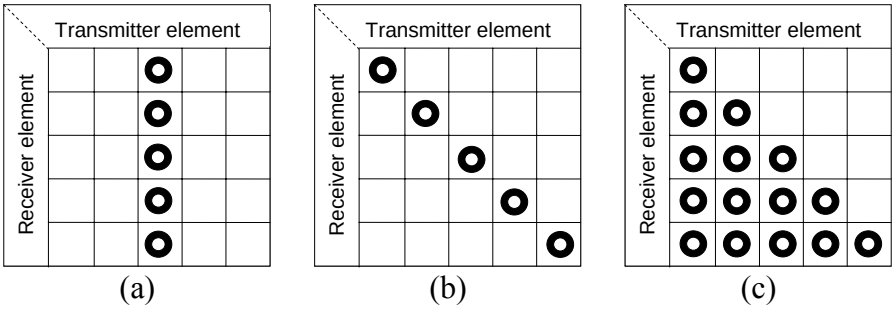

Figure 1. Transmit-receive geometries for the three imaging algorithms, a mark indicates that a time trace is recorded for that transmitter-receiver pair: a) CSM (pitch catch); b) SAFT (pulse-echo); c) TFM (Full array)

For an N element array, the CSM requires only one firing but would require N parallel receiver amplifier channels to record the N time traces. The SAFT has N separate firings but requires only one multiplexed amplifier channel to record the N time traces. In order to record the N(N-1)/2 time traces with only N separate firings, the TFM requires N independently amplified receiver channels. The image formation time is proportional to the number of time traces used but, in NDE, it is the acquisition time which is the more important factor. If image formation time is important then the imaging algorithms can be implemented faster by making extensive use of Fast Fourier Transforms and processing in the temporal and spatial frequency domains as was proposed for SAFT by Busse [8] and used in [2].

Theoretical Resolution of Algorithms

Imaging algorithms seek to create a representation of the object space in the image space. Ideally, if there was a point scatterer in the object space then this would appear as a point, or Dirac delta function in the image space. This is not the case when imaging with propagating waves since it is not possible to focus all of the acoustic energy to a point in the object space due to diffraction effects. Hence, there exists a physical limit to the spot size of the response of the imaging algorithms to a point scatterer. This response is known as the Point Spread Function (PSF). In microscopy, the imaging system is space invariant which means that the PSF is the same for every point in the object space. In this situation the image is simply the convolution of the PSF with the real object function. However, since we are concerned with focusing of the acoustic energy at various distances from the array aperture, we find that the PSF is not space-invariant and its size varies as the distance of the point scatterer from the array is changed.

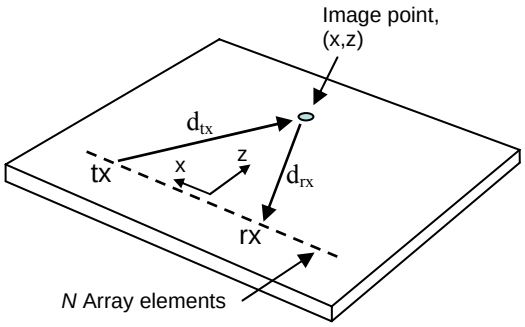

Figure 2. Geometry of the array setup

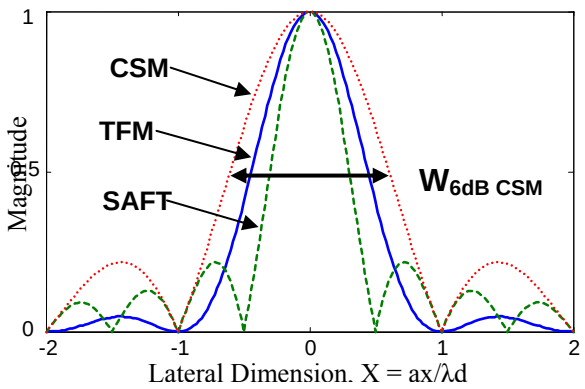

Figure 3. The theoretical PSF for CSM, SAFT and TFM

Here, we are interested in the lateral response, parallel to the array aperture, of the imaging algorithms. The lateral response to a point scatterer in the object plane is found to be a *sinc* function (*sinc(X) = sin(X)/X*). This shape occurs due to the effective low-pass filtering of spatial frequencies by the array aperture [9]. Assuming that the point scatterer lies on the optical axis then the modulus of the PSF for the CSM is:

$$h_{CSM}(x) = \frac{a}{\sqrt{d}}\left|\mathrm{sinc}(\pi X)\right|, \tag{3.a}$$

and

$$X = \frac{ax}{\lambda d}, \tag{3.b}$$

where x is the lateral dimension in the object plane; a is the array width; d is the distance of the point scatterer from the array; λ is the wavelength of the interrogating signal. The normalised PSFs plotted against the parameter X for the CSM and the other algorithms are shown in figure 3. In order to arrive at (3) we have had to make the approximation that the point scatterer is sufficiently far from the array aperture so that:

$$\sqrt{d^2 + \left(\frac{a}{2}\right)^2} \approx d\left[1 + \frac{1}{2}\left(\frac{a}{2d}\right)^2\right]. \tag{4}$$

For the SAFT algorithm, we record only the pulse-echo data and so $d_{tx}(x,z)$ is equal to $d_{rx}(x,z)$ and hence there appears a factor of two in the exponent of (2). This has the effect of doubling the spatial frequencies available for the construction of the image and hence halves the width of the PSF:

$$h_{SAFT}(x) = \frac{a}{\sqrt{d}}\left|\mathrm{sinc}(2\pi X)\right|. \tag{5}$$

The TFM algorithm contains summations over both transmitter locations and receiver locations. It is equivalent to dynamically focusing a wave beam at each image point in turn and hence is sometimes referred to as the Synthetic Phased Array (SPA) method [10]. The summations are separable and each one would produce an image the same as the CSM. In this way the TFM PSF is the square of the CSM PSF:

$$h_{TFM}(x) = \left(\frac{a}{\sqrt{d}}\mathrm{sinc}(\pi X)\right)^2. \tag{6}$$

We can characterise the PSFs of the three imaging algorithms in terms of the width of the main lobe and the magnitude of the sidelobes, which are classed as coherent noise. The ideal PSF, as stated above, would be a Dirac delta function which has an infinitesimal main lobe width and no sidelobes. One way of characterising the resolution of the imaging system is to measure the Full Width at Half Maximum (FWHM), also known as the 6dB width, W_{6dB} which quantifies the width of the PSF main lobe. We note that *sinc(X)* = 0.5 when $X = 1.88$. Therefore for the CSM we find W_{6dB} thus:

$$\pi\frac{ax_{6dB}}{\lambda d} = 1.88, \tag{7.a}$$

giving

$$W_{6dB} = 2x_{6dB} = 1.2\lambda\frac{d}{a}. \tag{7.b}$$

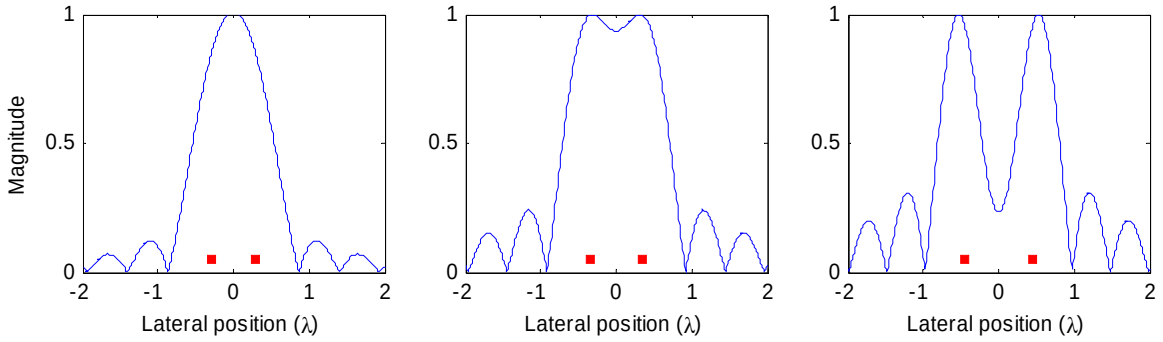

(a) (b) (c)

Figure 4. SAFT PSF with a=8λ and two point scatterers at d=8λ. The separation of the two scatterers is: a) 0.6λ < Sparrow separation ; b) 0.7λ = Sparrow separation ; c) 0.9λ > Sparrow separation.

The SAFT PSF has half the width of the CSM PSF. To find W_{6dB} for the TFM we note that $sinc^2(X) = 0.5$ when $X = 1.4$ and hence by the same process as (7), $W_{6dB} = 0.89\,\lambda d/a$. The FWHM are summarized in Table 1.

Another criterion for evaluating an imaging system is to measure its ability to distinguish two point scatterers. This criterion is often simply referred to as 'resolution'. Here, we choose the Sparrow separation to define the two point resolution. The Sparrow separation is the distance between two point scatterers at which a dip starts to appear in the image between the two point scatterer locations. Figure 4 shows the PSF for the SAFT algorithm with 2 point scatterers placed 8λ from the array and using an aperture of 8λ for three different scatterer separations. The scatterers are not distinguishable when their separation is 0.6λ but are resolved, in this case, when they are separated by more than 0.7λ. Table 1 compares the three algorithms in terms of W_{6dB}, first sidelobe amplitude and Sparrow separation.

Table 1. Theoretical W_{6dB}, first sidelobe amplitude and Sparrow separation for CSM, SAFT and TFM.

Algorithm	CSM	SAFT	TFM
W_{6dB}	$1.2\lambda\frac{d}{a}$	$0.6\lambda\frac{d}{a}$	$0.89\lambda\frac{d}{a}$
Sparrow separation	$1.4\lambda\frac{d}{a}$	$0.7\lambda\frac{d}{a}$	$0.9\lambda\frac{d}{a}$
Sidelobe amplitude	0.22 (-13dB)	0.22 (-13dB)	0.05 (-26dB)

Plate Experiments

Experiments were carried out on a 0.9mm thick mild steel plate using the fundamental flexural mode (A0). A PZT disc was used for excitation and was manually scanned to simulate a transduction array. The transducer disc was 2mm thick, had a diameter of 5mm and was bonded to a 6mm thick brass backing mass of the same diameter to increase input power to the plate. The transducer was held in place by a light spring. The PZT disc acts as an omni-directional point source for the A0 guided wave. The Poisson effect in the PZT disc may also cause some excitation of the S0 extensional mode but this is greatly reduced by fluid coupling the transducer to the plate since the fluid does not support shear forces.

The reflected field was measured using a heterodyne laser interferometer which was scanned across a line in front of the transduction line to simulate a receiver array. The laser is angled perpendicular to the plate so it only records out-of-plane movement which greatly reduces its sensitivity to the S0 wavemode which has very little out-of-plane motion. The reflected signal was recorded at all receiver locations for all source locations for full-array capture. The time traces recorded were averaged over 200 samples to sufficiently remove random noise. A five cycle Hanning toneburst centred at 50 kHz was used for the excitation signal. At 50 kHz, the A0 wavelength is 14mm.

In order to validate the theoretical results for the point spread functions a single brass rod of diameter 5mm was bonded to the surface of the plate. The rod creates a local change in acoustic impedance and hence causes a reflection of some of the input wave energy. Measurements were taken 108mm (7.7λ) from the target using an aperture of 56mm (4λ) and aperture sampling of 7mm (λ/2). In another experiment, two 5mm (0.35λ) holes were drilled through the steel plate. The centres of the holes were separated by 11mm (0.78λ). Two more plate experiments were then carried out using through-thickness slits as targets. The slits were cut parallel to the array aperture and had lengths of 11mm (0.78λ) and 35mm (2.5λ). Both slits were 1mm wide (0.07λ). Table 2 shows the geometry of all the experiments with lengths normalised to the wavelength of the A0 wavemode at 50 kHz.

Table 2. Geometry of the experiments. All distances in wavelengths.

Target	**Synthetic aperture (a)**	**Aperture sampling**	**N**	**distance to target (d)**	**d/a**
1 brass rod	4 λ	0.50 λ	9	7.7 λ	1.93
2 drilled holes	10 λ	0.50 λ	21	7.7 λ	0.78
11mm slit	10 λ	0.36 λ	29	10.0 λ	1.00
35mm slit	10 λ	0.36 λ	29	10.0 λ	1.00

Experimental Results

The data from the experiments was processed with the imaging algorithms in the frequency domain (2) using 17 discrete frequencies from 40-60 kHz. The phase velocity dispersion was measured experimentally and the measurements showed excellent agreement with DISPERSE predictions.

The response to the rod ‘defect’ was very similar to the predicted response to a point scatterer. The images are shown in figure 5 and the lateral section through the image peak in figure 6.a. The predicted 6dB widths for this experiment were 2.31λ, 1.16λ and 1.71λ for the CSM, SAFT and TFM respectively. The 6dB widths measured from the images were 2.13λ, 1.07λ and 1.55λ. The measured 6dB widths are slightly less than the prediction due to the broadband processing which contains information from frequencies higher than 50 kHz and hence of slightly smaller wavelength. Note that the lateral section shapes in figure 5.a are almost identical to the theoretical PSFs of figure 2. Also note the greatly reduced sidelobes in the TFM image (figure 5.c) and lateral section (6.a).

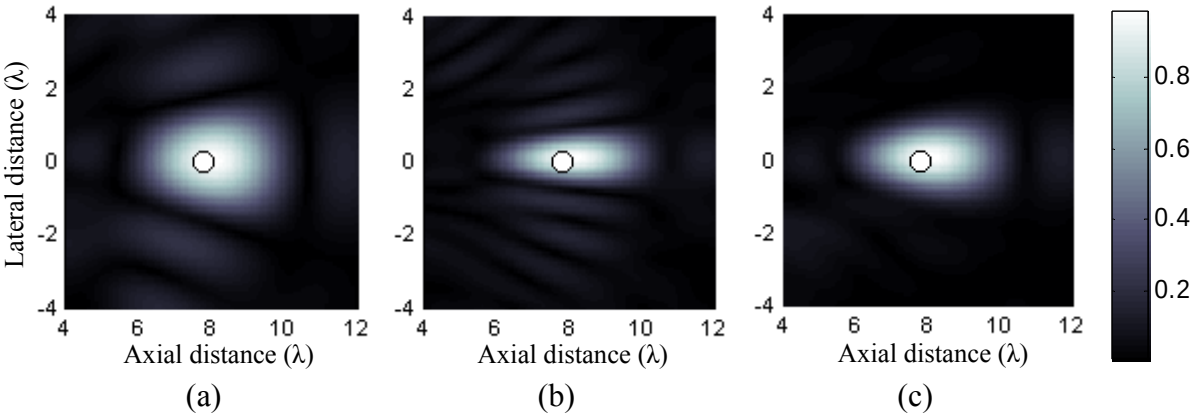

Figure 5. 1 rod scatterer: Image of area around the point scatterer (shown as white spots) which was 7.7λ from a 4λ aperture: a) CSM; b) SAFT; c) TFM.

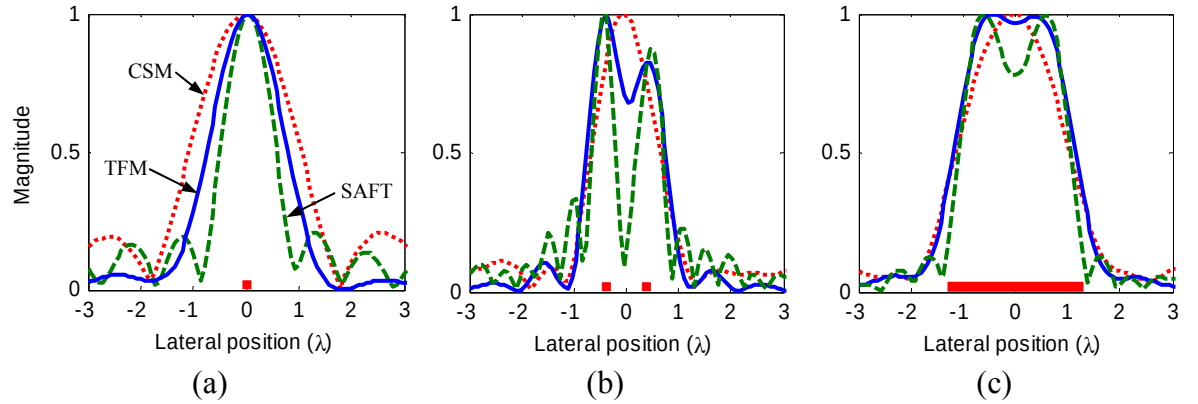

Figure 6. Lateral section through the image peak: CSM (·····); SAFT (-----); TFM (——): a) 1 rod scatterer; b) 2 drilled holes; c) 35mm (2.5λ) slit.

The images for the two-hole experiment are shown in figure 7. For this experiment d/a = 0.78. We therefore predict the Sparrow separation to be 1.09λ, 0.55λ and 0.9λ for the CSM, SAFT and TFM respectively. The actual separation of the holes was 0.8λ and hence we predict that the CSM will not resolve the two holes, the SAFT should easily resolve the two holes and the TFM will just be able to resolve them. This is shown clearly in the experimental lateral section through the image peak in figure 6.b. Also note the reduced sidelobes of the TFM image.

The 11mm slit images appear as if the slit were a point scatterer with the measured 6dB widths being those predicted for a point scatterer. Hence, we do not show the images in the paper. The measured W_{6dB} were 1.26 λ for the CSM, 0.88 λ for the SAFT and 0.64 λ for the TFM. The predicted W_{6dB} for the point scatterer case are 1.2 λ, 0.9 λ and 0.6 λ respectively.

The images created from the 35mm (2.5λ) slit experiment are shown in figure 8 and the lateral section through the image peak in figure 6.c. It can be seen that the CSM does not produce a realistic image of the lateral profile of the slit. The SAFT appears to be imaging the tip diffraction, showing two clear peaks. The TFM image is the most realistic representation of the lateral profile of the slit.

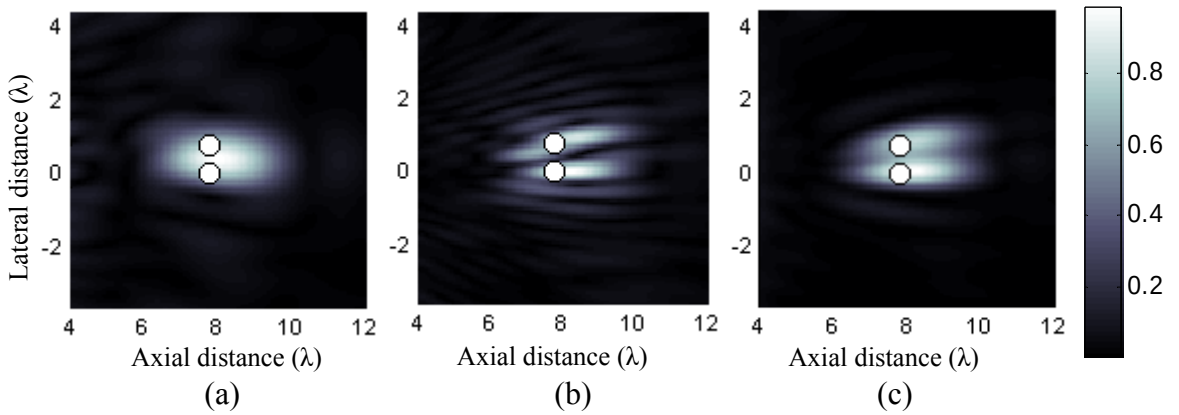

(a) (b) (c)

Figure 7. 2 drilled holes: Image of area around the holes (shown with white spots) which were of 0.8λ apart and 7.7λ from a 10λ aperture: a) CSM; b) SAFT; c) TFM.

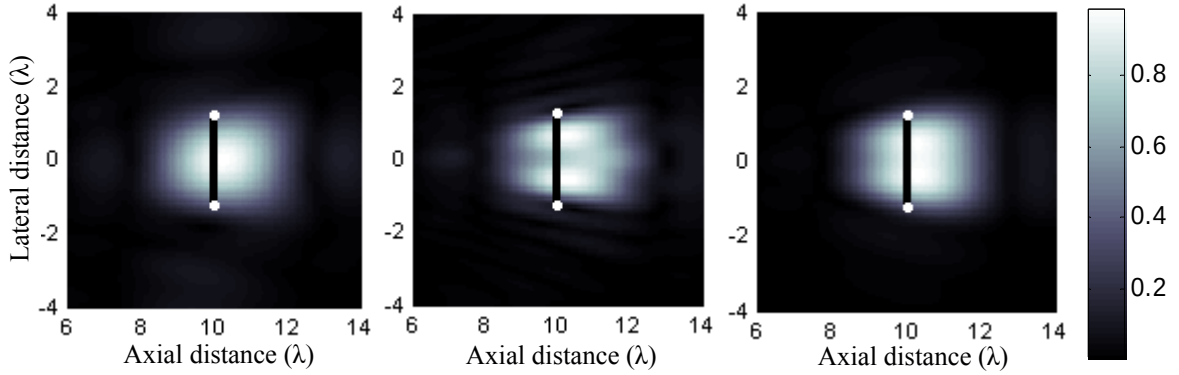

(a) (b) (c)

Figure 8. Image of area around the slit (black line with white tips) which was 2.5λ (35mm) long and 10λ from a 10λ aperture: a) CSM; b) SAFT; c) TFM.

Conclusions

Three synthetically focused imaging algorithms have been investigated theoretically and experimentally, the experiments validating the theoretical predictions. The response to a point scatterer was evaluated and it was found that SAFT has the narrowest point spread function, having half the width of the CSM PSF. SAFT also has the best two point resolution, being able to resolve two point scatterers placed with a lateral separation of $0.7\lambda d / a$. However, the TFM has significantly lower sidelobe amplitude than the CSM and SAFT making a much 'cleaner' image. The TFM requires significantly more data to be acquired and processed but the acquisition time can be the same as for SAFT if parallel reception across the array is possible. The TFM produced the most realistic image of the through-thickness slit, since the SAFT appears to be imaging mainly the tip diffraction.

References

1. Waszak, J., Ludwig, R., *IEEE Trans. Instrum. Meas.* **39,** 441-444, (1990).
2. Sicard, R., Chahbaz, A., Goyette, J., *IEEE Trans. Ultrason. Ferroelec. Freq. Cont.* **51,** 1287-1297, (2004).
3. Wilcox, P.D., *IEEE Trans. Ultrason. Ferroelec. Freq. Cont.* **50**, 699-709, (2003).
4. Karaman, M., Li, P., O'Donnell, M., *IEEE Trans. Ultrason. Ferroelec. Freq. Cont.* **42**, 429-441, (1995).
5. Holmes, C., Drinkwater, B.W., Wilcox, P.D, *Insight.* **47** issue 2, 88-90, (2005).

6. Wilcox, P.D., *IEEE Trans. Ultrason. Ferroelec. Freq. Cont.* **50**, 419-427, (2003).
7. Pavlakovic, B., Lowe, M.J.S., Alleyne, D.N., Cawley, P. *Review of Progress in quantitative NDE.* **16**, 185-192, (1997).
8. Busse, L.J., *IEEE Trans. Ultrason. Ferroelec. Freq. Cont.* **39**, 174-179, (1992).
9. Goodman, J.W., 'Fourier Optics', *McGraw-Hill*, publisher, London, UK (1996).
10. Chiao, R.Y., *IEEE Trans. Ultrason. Ferroelec. Freq. Cont.* **41**, 484-493, (1994).